Received 7 March 2025; Accepted 19 October 2025
https://doi.org/10.48612/letters/2025-4-297-303
https://elibrary.ru/ffycoi

Statistical characteristics of prismatic dislocation loops coagulating by glide and conservative climb

T. N. Aliev

alievtn@lebedev.ru

Lebedev Physical Institute of Russian Academy of Science "FIAN", Moscow 119991, Russia
Scientific Research Center "Kurchatov Institute", Moscow 123182, Russia

Abstract: Thermal exposures on metallic structural materials used in the nuclear industry may involve microstructural changes. As modeling and experiments have shown, the coarsening process of radiation-induced prismatic loops in the course of thermal annealing results in greater spatial homogeneity and stability of deformation when followed by plastic loading. On the other hand, loop coarsening deteriorates the material's resistance to thermal creep. In the operating temperature range used for structural materials in nuclear applications, the volume diffusion of vacancies is small. The change in the loop's size and density occurs due to the migration caused by elastic interactions. As glide results in trapped configurations, the slower process of conservative climb is a key recovery process under these moderate temperatures. The article presents the Monte Carlo modeling of the evolution of prismatic loop statistic parameters in the course of annealing with varying initial shares of vacancy loops. The radial correlation function normalized to the average interloop distance becomes time-independent after the loop concentration decreases by half. The calculation results are used to construct equations for the change in concentration, radial correlation function, and size distribution function of prismatic loops during coagulation involving glide coupled with conservative climb. The evolution of the size distribution function and the change in the relative number of dominant type of loops can serve as an auxiliary tool to verify the nature of the loop coarsening process in specific experiments, along with the traditional evaluation of activation energy from the changes in the loop's concentration and mean size.

Keywords: Monte Carlo, prismatic loops, conservative climb, coagulation, coalescence

1. Introduction

The parameters of prismatic radiation-induced loops affect the mechanical properties of candidate materials for thermonuclear energy [1, 2] and classic materials in thermal nuclear reactors [3]. Thermal exposures on the material in abnormal situations, accidents or during spent fuel storage lead to the loop coarsening. The mobile dislocations interact with prismatic loops in an elastic or inelastic manner, depending on the relation among the dislocation line, Burgers vectors of the dislocation and the loop [4 – 6].

Modeling of dislocation motion in deforming material with spaced prismatic loops shows that the deformation channeling and, as a result, the macroscopic instability of deformation increases with the total loop area [5, 7]. External stress may convert large enough prismatic loops into dislocation sources [8]. Therefore, the loop size distribution function (SDF) is important in dislocation dynamics modeling (DDM).

At high temperatures, the coarsening of loops proceeds by the Ostwald ripening involving vacancy bulk diffusion. The self-similar SDF for Ostwald ripening is found in classical works, while the transition stage is modeled in DDM [9]. In the operational temperatures for materials in nuclear power engineering, the bulk diffusion of vacancies is mostly insignificant as materials are chosen to maintain phase and dimensional stability. The online TEM study of the prismatic loop migration in [10] in γ-irradiated samples of Zr-0.1 Fe at 400°C and BCC iron [11] at 500°C has shown that the effective activation energy of annealing is lower than the activation energy for vacancy self-diffusion. Also, the loops SDF [3,12] differs from that found for Ostwald ripening [9].

Homogeneous stress only rotates loop's habit plane. Stress gradient imposed by the other loop causes gliding along the Burgers vector. Estimates of the segregation effects on the glide mobility of loops in irradiated tungsten have shown that loops larger than 6 nm [13] are not trapped at a typical loop density of $10^{(22\div23)}$ m^{-3}.

At higher temperatures the loop motion becomes 3-dimensional: the loop drifts in its habit plane due to the transfer of vacancies along the dislocation core, known as the self-climb. It results in a slow coagulation after loops have glided into trapped configurations. The mobility in self-climb is analytically studied in [14,15]. DDM in [11] gave the values for the activation energy Q as $2E_m$ and $2.5E_m$ for <111> and <100> loops in BCC metals (where E_m is the migration energy of a vacancy), whereas the activation energy of self-diffusion in the Ostwald coalescence is $E_{SD} = E_f + E_m = (3 \div 5)E_m$ for BCC and $E_{SD} = (2 \div 3)E_m$ for FCC metals (E_f — formation energy). Also, the observed activation energy of loop annealing is $(0.4 – 0.7)E_{SD}$ for many materials [11].

The first formulations for DDM for glide and self-climb have been developed only recently [16,17]. In [16] the coalescence of closely spaced prismatic loops is modeleed. In [17], the bulk transport of vacancies was added. DDM is useful when loop spacing is comparable with their diameter.

At the mesoscopic level, there is a lack of applied results for the behavior of the loop ensemble. This article presents the numerical modeling for the loop motion by the glide and conservative climb in the dipole approximation. The model is used to construct equations for the loop density and size distribution. This model could be used to evaluate the loop's mobility from experimental data. Also, the model could provide input parameters in modeling the annealing effects on the plasticity of irradiated materials.

2. Methods

Analytical results for the mobility and interaction for round loops are used in the model. The mobility of a loop with radius R_1 by self-climb in its habit plane is [15]:

$$M = D'\delta^2 b\left(\pi kTR_1^{\,3}\right)^{-1}, \qquad (1)$$

where D' is the mostly unknown diffusion coefficient along the dislocation line ("pipe diffusion"), δ is the radius of the dislocation core, and b is the value of the Burgers vector. For D' parameter the notation is used $D' = \nu b^2 \exp(-Q/(kT))$, where $\nu \sim 10^{13}$ s^{-1} is the frequency of atomic jumps, Q is the activation energy of pipe diffusion, δ may be evaluated as the value of the Burgers vector b [15], k is a Boltzmann constant, T is a temperature, so Eq. (1) may be written as:

$$M = \nu b^5\left(\pi kTR_1^{\,3}\right)^{-1}\exp\left(-Q/kT\right). \qquad (2)$$

In the dipole approximation, valid for distance r between loop centers much larger than their diameters, the interaction energy of two loops of area A_1 and A_2, is [18]:

$$E_{\text{int}} = \frac{\mu b_1 b_2 A_1 A_2}{4\pi(1-\upsilon)r^3} E_0(\bar{n}_1, \bar{n}_2, \bar{b}_1, \bar{b}_2, \bar{r}), \qquad (3)$$

where μ is the shear modulus, υ is the Poisson's ratio, A_i (i=1, 2) is the area of the loop with radius R_i, $\bar{n}_1$, $\bar{n}_2$ are unit vectors normal to loop's surfaces. Vectors in Eq. (3) are shown in Fig. 1.

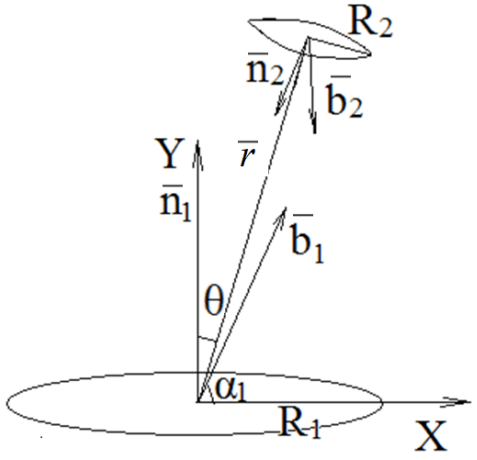

Fig. 1. Shematic configuration of two interacting loops.

Force acting on the loop:

$$F_i = -\partial\left(\sum_{j\neq i} E_{\text{int}}(r_i - r_j)\right)\Big/\partial r_i. \qquad (4)$$

The expression for $E_0(\bar{n}_1, \bar{n}_2, \bar{b}_1, \bar{b}_2, \bar{r})$ is provided in [18]. To facilitate the analysis, loops are assumed to be prismatic and coplanar:

$$\bar{n}_1 = \bar{n}_2 \,||\, \bar{b};\ b_1 = \pm b_2. \qquad (5)$$

In this case [18]:

$$E_0 = \left(15\cos^4\theta - 6\cos^2\theta - 1\right), \qquad (6)$$

where θ is the angle between the normal and the vector $\bar{r}$ (see Fig. 1). The velocity is

$$d\bar{r}/dt = M_{\text{cl}}\left(\bar{F} - \left(\bar{b}\times\bar{F}\right)\bar{b}/b^2\right) + M_{\text{gl}}\left(\bar{b}\times\bar{F}\right)\bar{b}/b^2, \qquad (7)$$

where M_{gl} and M_{cl} are the mobilities for glide and climb in the direction of the Burgers vector and normal to it. Monte-Carlo calculations are based on previous equations and on the conservation of the number of defects in coagulation events.

In the Monte-Carlo model, loops with the same Burgers vector direction but different signs are spaced in a 1 μm cube. Periodic boundary condition is applied. Each loop experiences the sum of forces from other loops (Eq. (4)) and moves with a velocity (Eq. (7)). If two loops approach each other at a distance smaller than their predicted flight per the next step they are treated as reacting. The area of the new loop comes from the conservation of matter with a positive sign ascribed to interstitial-type and a negative sign to vacancy-type. The time step is a fraction (≈0.03) of the characteristic recombination time for the current loop density. The ratio of mobilities for glide and self-climb is fixed as a constant.

3. Results

3.1. Pair interaction

Figure 2 shows the set of trajectories for the motion of two loops with the Burgers vector directed vertically. In each set, two loops are initially spaced in the centrally-symmetric configuration marked as empy blue circles with line connecting them inclined by various angles to axes. Two zones are separated by a "separatrix", shown as a dashed line. In first zone loops migrate to the limiting trajectory followed by travel to a coagulation event. In the second zone loops move away from each other. With an increase in the $M_{\text{gl}}/M_{\text{cl}}$ or ease of glide (results not shown in Fig. 2), the loops are leaning quicker to the limiting trajectory, but the limiting trajectory itself and the separatrix is the same as in Fig. 2.

The motion of two loops in their habit plane at a distance x between their centers defines the scaling parameter κ s^{-1} [15]:

$$d\left(x/b\right)^5/dt = -\left(R_{\text{eff}}b^{-1}\right)\kappa, \qquad (8)$$

$$\kappa = \left(\frac{\mu b^3}{kT}\right)\frac{15\nu}{2(1-\upsilon)}\exp\left(-\frac{Q}{kT}\right), \qquad (9)$$

where the effective radius:

$$R_{\text{eff}} = \left\{R_1^{-3} + R_2^{-3}\right\}R_1^{\,2}R_2^{\,2}/2. \qquad (10)$$

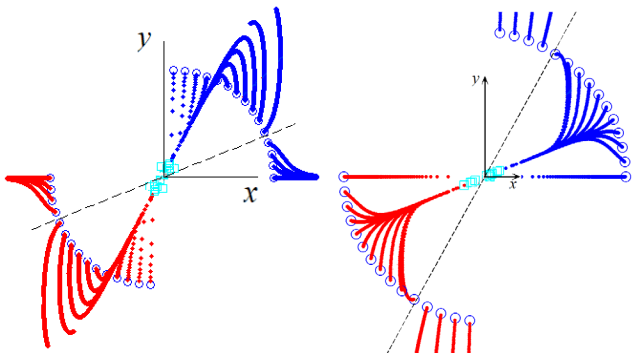

Fig. 2. (Color online) Successive positions of a pair of loops with $M_{gl}/M_{cl}=4$, initially spaced in the centrally-simmetryc configurations (various pairs with different inclination to axis are presented) at blue circles: left — for two loops of different signs and on the right — for loops of the same sign. The loop normal and the Burgers vector are parallel to the *y*-axis; the cyan squares are the coagulation points.

For loops spaced at distance *r*, the reference recombination time $\tau_{reg}(r)$, also viewed as the inverse of the reference recombination frequency $f_0^{-1}(r)$:

$$f_0^{-1}(r)=\tau_{req0}(r)=\kappa^{-1}(r/b)^5\cdot(b/R_{eff}). \qquad (11)$$

The calculated recombination times in units τ_{reg0} for different angles θ between the *y*-axis and the line connecting initial loop positions are given in Table 1.

The inverse recombination time, or frequency *f*, is defined by averaging over the directions of loop arrival on a unit sphere:

$$f/f_0=\tau_{req0}\left\langle\tau(\theta)^{-1}\right\rangle= =\tau_{req0}\left(\int_0^{\pi/2}d\Omega\right)^{-1}\int_0^{\pi/2}\left(\tau(\theta)\right)^{-1}P(\theta)d\Omega(\theta). \qquad (12)$$

Here $P(\theta)d\theta$ is the probability of the loop arriving in the range of angles $d\theta$; the solid angle is:

$$\Omega(\theta)=2\pi(1-\cos(\theta/2)). \qquad (13)$$

The averaging Eq. (12), assuming an isotropic distribution of incoming loops ($P(\theta)=1$) gives (the index "+ –" for loops of different signs, "+ +" for loops of the same sign):

$$f_{+-(M_{gl}/M_{cl}=4)}=2.7f_0;\quad f_{+-(M_{gl}/M_{cl}=10)}=3.4f_0;\quad f_{++(M_{gl}/M_{cl}=4)}=f_{++(M_{gl}/M_{cl}=10)}=1.7f_0. \qquad (14)$$

3.2. Ensemble of loops

In order to describe an ensemble of loops, it is useful to introduce the radial correlation function of loops ρ(RCF) as the ρ*dr* is the probability of finding the nearest loop in the interval [*r*, *r*+*dr*]). The RCF for initial random spacing is easily obtained. The condition that no loops fall into some volume $V<<V_T$ (where *N* loops are randomly spaced in reservoir volume V_T):

$$P_{V,null}=\left(1-V/V_T\right)^N\approx\exp\{-Vn\}. \qquad (15)$$

Here *n* is the volume concentration, m^{-3}. Then the initial RCF is the product of Eq. (15) and the probability of finding a random loop in spherical layer *dr*:

$$\rho_{rand}(r)=\exp\left\{-\left(4\pi/3\right)r^3n\right\}4\pi r^2n. \qquad (16)$$

Monte-Carlo simulations have shown that the RCF becomes time-independent after the total loop density is decreased twice from the initial value. Initial RCF (say, random or periodic) affects only the time to reach stationary RCF. Ordering also shows up in progressive concentration of the nearest loop (to any selected) either with ≈70° if it has the same sign as a selected loop or 30°, if it has an opposite sign. It is a natural result of attraction to stationary directions in pairwise interaction, shown in Fig. 2.

This RCF has two zones. In the near zone $r<r^*$, the interaction can be considered as pairwise. The near zone solution follows from the flux conservation:

$$\left(dr/dt\right)\rho(r)=\left\langle f\right\rangle/2, \qquad (17)$$

where <*f*> is an average value of *f* (Eq. (14)) weighted with the share of respective reactions. The factor ½ comes from the fact that, excluding the case of coagulation with two equal-sized and opposite-signed loops, coagulation produces one particle per two reacted, effectively eliminating ½ loop per each reacted. The velocity comes from Eq. (8)

$$\left(dr/dt\right)=r^{-4}b^5\left(\kappa/5\right)\left(R_{eff}/b\right). \qquad (18)$$

So, in $r<r^*$:

$$\rho(r)_{r<r^*}=\left(\left\langle f\right\rangle/2\right)r^4\left[b^5\left(\kappa/5\right)\left(R_{eff}/b\right)\right]^{-1}. \qquad (19)$$

The stationarity of normalized RCF ρ′ means that it is a function of

$$r'=rn^{1/3}. \qquad (20)$$

So, the normalized capture radius is a constant to be found using ρ′(*r*′):

$$r^*(n)^{1/3}=\alpha. \qquad (21)$$

Table 1. Recombination times in units τ_{req0} calculated for glide/climb mobilities $M_{gl}/M_{cl}=10$ or 4 and for loops of either the same or different signs.

θ, °	6	18	24	30	36	42	48	54	60	66	78	90
$M_{gl}/M_{cl}=4$*	-	-	-	0.19	0.09	0.11	0.16	0.22	0.29	0.37	0.51	0.62
$M_{gl}/M_{cl}=10$*	-	-	-	0.33	0.18	0.18	0.21	0.26	0.32	0.38	0.51	0.62
$M_{gl}/M_{cl}=4$**	0.028	0.06	0.115	0.24	0.49	0.93	1.65	-	-	-	-	-
$M_{gl}/M_{cl}=10$**	0.016	0.037	0.09	0.22	0.475	0.94	1.56	2.5	-	-	-	-

* and ** — loops of the same sign and of opposite sign, respectively

Rewriting Eq. (19) with f_0 from Eq. (11) gives:

$$\rho'(r') = 2.5\left(\langle f\rangle / f_0\right)\left(r'\right)^4 \alpha^{-5}, \qquad (22)$$

In simulations in Fig. 3, reactions among the same type of loops prevails, so Eq. (14) gives for $\langle f\rangle/f_0 \approx 1.7$. Finally, comparison of Eq. (22) with the fitted by the blue dotted line in Fig. 3 $\rho'(r') = \left(40 \pm 15\right)\left(r'\right)^4$, gives $\alpha = 0.63 \pm 0.05$.

Note that the value of α could not be obtained solely on analytical grounds, because boundary conditions for RCF's "near-zone" is governed by collective processes in RCF's "far-zone". Analytical approximation (23) (see Fig. 3) for he stationary RCF is used in Section S2 of Supplementary Material to find the loop size distribution function (SDF):

$$\rho'(r') = 1.09\exp\left(-15(r'-0.45)(r'-0.9) - 5\max\left\{0, r'-0.9\right\}\right). \qquad (23)$$

Now the kinetics for the system is:

$$\begin{aligned} \frac{dn_+}{dt} &= -\frac{n_+}{n}\left\{\frac{1}{2}n_+ f_{++} + n_- f_{+-}\right\} \\ \frac{dn_-}{dt} &= -\frac{n_-}{n}\left\{\frac{1}{2}n_- f_{--} + n_+ f_{+-}\right\} \end{aligned}. \qquad (24)$$

Here, n_+ and n_- are densities [m^{-3}] of positive and negative loops, respectively, the f_{++}, f_{--}, f_{+-} are recombination frequencies (Eq. 14) with f_0 defined by Eq. (11). The factors ½ at f_{--} and 1 at f_{+-} mean that opposite-signed loops of same radius annihilate, while merging of same-signed loops leaves one loop.

Adding and subtracting the two Eqs. (24):

$$\frac{dn}{ndt} = -\left(8n^2\right)^{-1}\left\{\left(n+\Delta\right)^2 f_{++} + \left(n-\Delta\right)^2 f_{--} + 4\left(n^2-\Delta^2\right) f_{+-}\right\}. \qquad (25)$$

$$\frac{d\Delta}{ndt} = -(8n^2)^{-1}\left\{\left(n+\Delta\right)^2 f_{++} - \left(n-\Delta\right)^2 f_{--}\right\}. \qquad (26)$$

where Δ is the difference between two types:

$$n_\pm = \left(n \pm \Delta\right)/2. \qquad (27)$$

As it is assumed in the Monte-Carlo simulations, the loop's mobility is indifferent to its sign (in general, it is not true), so

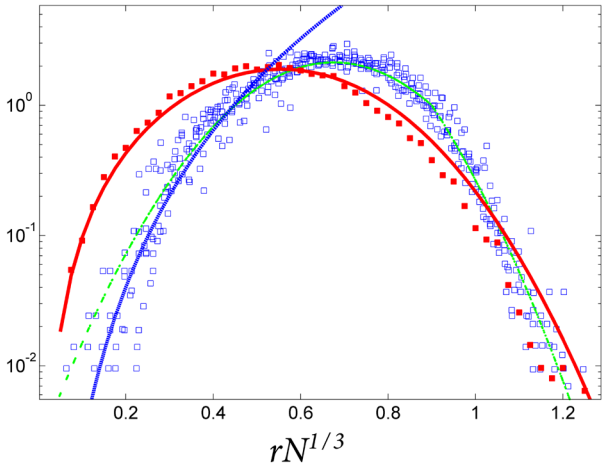

Fig. 3. (Color online) The value 4πr2ρ′ where ρ′ is the RCF at different annealing times. Symbols: ▪ — the initial RCF for random spacing; □ — RCF from numerical calculations in moments when $n(0)/n(t) = 3$, 6.8; 13.5; 28. Lines: the red solid is Eq. (16), the blue dotted is $\rho(r') = 40(r')^4$ — is the asymptotic for $r < r^*$. The green line is Eq.(23).

$f_{++} = f_{--} \approx f_{+-}$. The system (25) – (26) reduces to one equation in two subcases. If $\Delta_{t=0} = n$:

$$dn/dt = -nf_{++}/2 \qquad (28)$$

and if $\Delta_{t=0} = 0$:

$$dn/dt = -n\left\{f_{++} + 2f_{+-}\right\}/4. \qquad (29)$$

System (25) – (26) must be modified in the initial coagulation stage: the RCF is not stationary until the loop's density decrease twofold. The idea is to treat the system at time t as loops with an emptied sphere, or 'recombination volume' V_{rec} around it with radius r such that $t(r)$ is the recombination time defined in Eq. (11). Any initial loop in this sphere is considered as merged with the central one, so:

$$\frac{dn}{ndt} \approx -\frac{dV_{rec}}{dt}n = -\frac{4\pi}{3}\frac{dr^3}{d\tau_{req0}}n. \qquad (30)$$

Applying Eq. (11) to calculate $dr^3/d\tau_{req0}$ and using the same procedure, one comes to Eqs. (25) – (26) with prefactor f_0 within f_{++}, f_{+-} replaced with

$$f_0 \to n\left\{b^5\kappa(R_{eff}/b)\right\}^{3/5} t^{-2/5}. \qquad (31)$$

Validation of Eqs. (25) – (26) for "correlated" (i. e. with stationary RCF) stage of coagulation and Eqs. (25) – (26) with the replacement (31) for "uncorrelated", or initial stage, is shown in comparison with Monte-Carlo simulation results in Section S3 in Figs. S3.3 – S3.5.

3.3. Loop growth

In Eqs. (25) – (26) the effective radius is used through f (proportional to f_0 in Eq. (11)) parameters. Monte-Carlo calculations have shown that loops do not separate into growing immobile centers that attract smaller and thus mobile loops. It means that the statistical avarage (Eq. (10)) over the coagulation events is equal to the mean radius $\langle R\rangle$.

Loop size distribution provide usefull information on the coagulation process. In Sections S1 – S2 statistical model for the loop size distribution function (SDF) is formulated. This model treats any loop at a given moment t as a coagulation product of all loops spaced initially in a specific recombination volume. The mean value of recombination volume is equal to the inverse density of loops, i. e., n^{-1}. The radius of this assumed volume is statistically distributed with the same distribution as the RCF shown in Fig. 3, as long as RCF is a distribution for the radius of the largest empty sphere around the loop. Validation of the SDF model is provided in Section S3 by comparison with Monte-Carlo simulation results.

For applications one may consider two simple initial situations: 1) only one type of loops is present 2) equal number of positive and negative loops.

For the first case, the matter conservation gives:

$$\left\langle R^2(t)\right\rangle^{1/2} = R_0\sqrt{n_0/n}. \qquad (32)$$

Substituting it as $\langle R\rangle \approx \left\langle R^2\right\rangle^{1/2}$ into Eq. (11) for f_0 and then into Eq. (28) results:

$$dn/dt = -\left(1/2\right)\left(f_{++}f_0^{-1}\right)n^{13/6}\kappa b^4 R_0\sqrt{n_0}. \qquad (33)$$

The integration gives

$$n/n_0 = \left(1 + \left(7/12\right)f_{++}f_0^{-1}\kappa b^4 R_0 n_0^{10/6} t\right)^{-6/7}. \qquad (34)$$

For the second case, an area of a given loop is a sum of n_0/n loops with area $\pm\pi R_0^2$ with a random sign. As in the one-dimensional diffusion in the space of loop's area:

$$\left\langle R^2(t)\right\rangle \approx R_0^2\sqrt{n_0/n}. \quad (35)$$

And in a similar way as Eq. (34) one obtains

$$n/n_0=\left\{1+17/48\left(\left(f_{++}+2f_{+-}\right)f_0^{-1}\right)\left\{\kappa b^5\left(R_0/b\right)n_0^{10/6}\right\}t\right\}^{-12/17}. \quad (36)$$

One may use Eqs. (32) and (35) as an upper and lower estimate for mean loop radius if loop's share is not known. Otherwise, averaging SDF proposed in Sections S1 and S2 is recomended.

4. Discussion

To demonstrate the viability of the model, let's apply it to the data on post-reactor annealing of zirconium alloys. Isothermal annealing [3] was performed on M5 (Zr-1Nb-O) alloy samples cut from fuel claddings irradiated for 5 years in a PWR reactor. For the as-irradiated and annealed materials, loop parameters were identified by sampling $20\div40$ loops [3]. The initial loop density was $(1.2\pm0.4)\cdot10^{22}$ m^{-3}, mean radius $\approx6\pm2$ nm with 50% being of vacancy type. Elastic moduli and activation energy $Q=1.65$ eV in the calculation were set the same as in [20], while the jump frequency was set to $\nu_0=3\cdot10^{13}$ s^{-1}.

Analytical model results for vacancy loop share 1/2 (dashed lines) and 1 (solid lines) are shown in Fig. 4 [3]. It is seen that data is closer to the $R\approx n^{-1/4}$, i. e., to the vacancy loop share 1/2 for 350°C and 400°C. Indeed, this parameter was constant at 350°C and grew up to 71% at 400°C [3]. At 450°C data is close to $R\approx n^{-1/2}$ (one type dominant), which is in accord with the observed extinction of interstitial loops [3].

Extinction of interstitial loops while they start with the same density as vacancy loops means that they had different initial SDF. To avoid this sensitive initial unknown, a Monte-Carlo simulation at 400°C was performed with parameters measured at 250 h of annealing taking as initials: number density, vacancy loops share of 65% and SDF (SDF used in the paper is extrapolated from the data [3] having histogram on the uniform r grid $f_{exp}(r)\Delta r$ to function $f((r/r_0)^2)\Delta(r/r_0)^2$ on uniform $(r/r_0)^2$ grid where r_0 is some chosen value). Also, another procedure is used to find Q with the demand of best fit to the SDF measured in the end, not density, i. e., after the second step of 250 h annealing. Candidate time moments were found with $n/n_0=3\div4.3$, giving $Q=1.57\div1.60$ eV. The calculated vacancy loop share increased from 65% to 68%, while it reached 71% in experiment [3]. A possible reason for the underestimation of the vacancy loop share is the unaccounted bulk diffusion. The later may result in faster dying out of the interstitial loops, as they are an ideal sink for vacancies emitted from small vacancy loops. Coagulation by elastic interaction is less sensitive to the type of loops, so it tends to underestimate the rate of loop share growth. This picture is qualitatively in accord with the results of modeling [3] performed for the experiment [3]. In [3] authors used the cluster dynamics simulation for the evaporation-condensation process among immobile loops with the vacancy self-diffusion activation energy taken as 2.4 eV [3]. The model [3] overestimates the rate of vacancy loop share growth by orders of magnitude [3] at 400°C starting with vacancy loops' prevalence in a few percent over interstitial loops. Also, the model [3] underestimates the annealing rate at 350°C and overestimates the initial rate at 400°C. Both these facts may come from the assumption [3] that Ostwald ripening was the main process.

Evaluating Q by fitting SDF is, in fact, fitting the loop radius growth. This procedure may be more accurate compared with the conventional analysis of kinetics if the loop density is known with large uncertainties. Also, the model not accounting for evaporation-condensation is less precise for the smallest loops and, as a result, for number density.

Another annealing experiment [12] used PWR fuel claddings with zircaloy-4 (Zr-1.5Sn-0.22Fe-0.11Cr, stress-relieved annealed) and zircaloy-2 (Zr-1.5Sn-0.15Fe-0.11Cr-0.06Ni, recrystallization annealed) [12]. Initial loop density was $(3.4\pm1.7)\cdot10^{22}$ m^{-3}. Modeling was performed with the assumed vacancy loop share of 1/2 and initial SDF functions provided in [12] (see Fig. 5). The first regime was 500 h hold

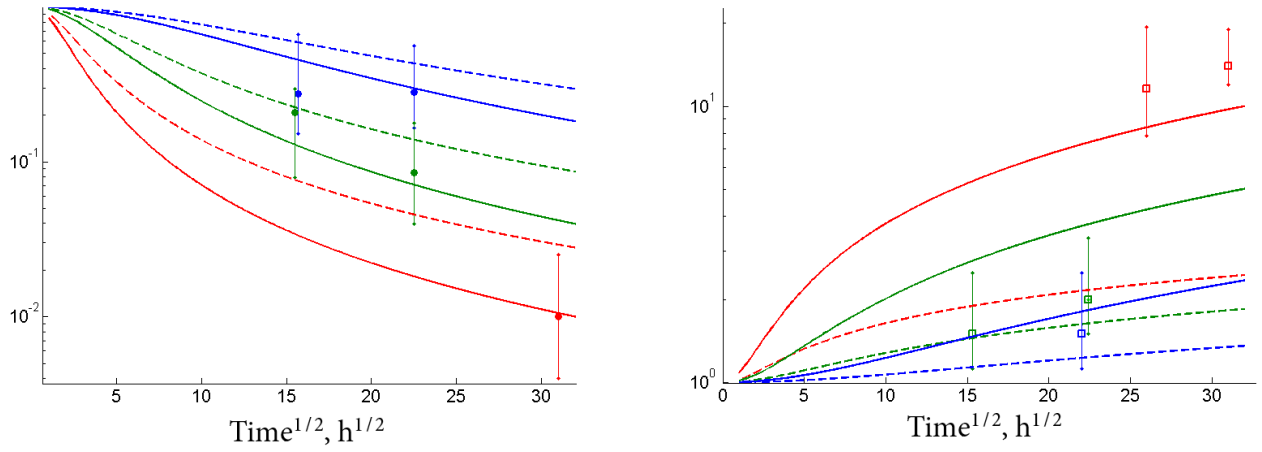

Fig. 4. (Color online) Relative change in density (left) and diameter (right) during annealing of M5 (Zr-1Nb-O) samples cut from fuel cladding irradiated in PWR reactor: 350°C — blue, 400°C — green, 450°C — red. Symbols — data [3]. Solid lines are Eq. (34) and (32) for the vacancy loop share 100% and dashed lines are Eqs. (36) and (35) for vacancy loops share 50%.

at 427°C, while the second and the third were isochronal holds $\Delta t = 5$ h starting from 343°C with increments of $\Delta T = 28$°C. The second and the third regimes ended at $T_i = 399$°C and $T_i = 510$°C, respectively. Since temperature in kinetic equations comes as a multiple $dt \cdot \exp(-QT(t)^{-1})$, it is easy to replace time with the integral of this multiple divided by $\exp(-QT_i^{-1})$, called an effective time at a T_i. The latter may be approximated as a geometric series, equal to $t_{eff} = (1 - \exp(-Q\Delta T T_i^{-2}))^{-1}\Delta t$. Effective time at 399°C and 510°C is $(1.39 \pm 0.04)\Delta t$ and $(1.66 \pm 0.05)\Delta t$ assuming $Q = 1.75 \pm 0.1$ eV. In Fig. 5, the calculated result is compared with $f((r/2.5\text{ nm})^2)$ obtained by extrapolation from data on $f(r)\,dr$ [12]. Resulting values of n_0/n for moments shown in Fig. 5 are presented in Table 2 together with data [12]. Value Q found by fitting to data on n_0/n or to SDF are also given in Table 2.

To summarize, given a value of vacancy jump frequency $\nu_0 = 3 \cdot 10^{13}$ s^{-1} (*ab initio* result is $1.8 \cdot 10^{13}$ s^{-1} for α-Zr [21]), the fitted pipe diffusion activation energy Q for Zr-Nb and Zr-Sn-Fe-Cr alloys is in the range 1.65÷1.95 eV. *Ab initio* results give 1.7÷1.9 eV for the E_f in a-Zr with the lower band evaluated as 1.5 eV [21,22]. The Q value must be higher than E_f by unknown migration energy in the dislocation core. On the other hand, alloying elements and impurities may lower E_f. The found value for Q may be compared with low-temperature (0.3 – 0.5 of melting temperature) creep activation energy, usually attributed to pipe diffusion [23]. In [24] activation energy in creep for a-Zr was found to be 1.7÷2.1 eV at 350 – 450°C, increasing upto 2.75 eV at higher temperatures. In [20] author proposed that the coagulation of loops emitted by super-jogs serve as a relieving process in zircaloy-4 creep at 400 – 500°C range. The creep model [20] value attributed to the coagulation was 1.65 eV while using somehow overestimated $\nu_0 = 1.4 \cdot 10^{14}$ s^{-1} [20].

5. Conclusions

A three-dimensional numerical model has been developed for the coagulation of round prismatic dislocation loops by glide and self-climb. This process may result in ripening of loops in irradiated metals and alloys under moderate temperatures when Ostwald ripening is not fast enough and given the dislocation motion is not too damped by alloying, segregation and impurities. Modeling for loops with one habit plane with their normal parallel to the Burgers vector has been used to construct an analytical model. Loops in the ensemble separate into loops moving in the collective field and those trapped in pairs while moving along stable trajectories. The kinetics of the concentration of interstitial and vacancy loops are described by two rate equations. The size distribution function (SDF) is found using the stationary RCF as a distribution for the radius of a sphere, emptied by coagulation. Analytical SDF as well as rate equations are verified against the numerical Monte-Calro model. Kinetics and SDF are verified against zirconium annealing data, adjusting the sole free parameter of the model — activation energy for pipe diffusion.

Table 2. Evaluation of Q parameter in the model with $\nu_0 = 3 \cdot 10^{13}$ s^{-1}.

		Fitted to data on n_0/n	Fitted to SDF data (Fig. 5)	
Annealing	n_0/n [12]	Q, eV	n_0/n calculated	Q, eV
Zircaloy-4, n_0 (3.42 ± 1.67) 10^{21} m^{-3}				
427°C, 500 h	3.14 (1.5÷9.4)	1.9 ± 0.1	3	1.92
510°C, t_{eff} 8.3 h	58 (22÷130)	1.56 ± 0.1	11.4	1.72
Zircaloy-2, n_0 assumed the same as for zircaloy-4				
427°C, 500 h	2.5 (1.2÷6.3)	1.94 ± 0.1	2	1.96
510°C, t_{eff} 8.3 h	10 (4÷22)	1.73 ± 0.1	5.3	1.8

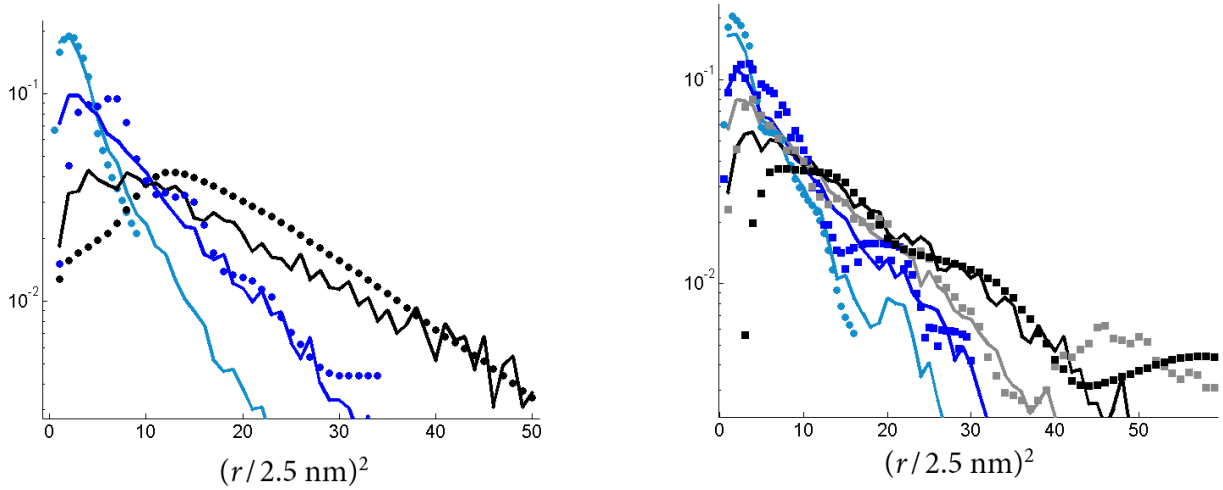

Fig. 5. (Color online) SDF as $f((r/2.5\text{ nm})^2)$ for zircaloy-4 (left) and zircaloy-2 (right) annealing: cyan — initial after irradiation in PWR as a fuel cladding, gray and black — after isochronal annealing with effective time evaluated (see text) as 7 h at 399°C (gray) and 8.3 h at 510°C (black), blue — after 500 h at 427°C. Points — data [12].

Supplementary material: *The online version of this paper contains supplementary material (appendices containing additional calculations and verification data) freely available at the journal's web site https://lettersonmaterials.com.*

References

1. J.-H. You, A review on two previous divertor target concepts for DEMO: mutual impact between structural design requirements and materials performance, Nucl. Fusion 55 (2015) 113026.
2. M.R. Gilbert, S.L. Dudarev, D. Nguyen-Manh, S. Zheng, L.W. Packer, J.-Ch. Sublet, Neutron-induced dpa, transmutations, gas production, and helium embrittlement of fusion materials, Journal of Nuclear Materials 442 (2013) S755 – S760.
3. J. Ribis, F. Onimus et al, Experimental and micromodelling approach of irradiation defects recovery in zirconium alloys: impact of an applied stress, J. ASTM International, 5, 3 (2008) 1 – 21.
4. G. Monnet, Multiscale modeling of irradiation hardening: Application to important nuclear materials, Journal of Nuclear Materials 508 (2018) 609 – 627.
5. H. Yuya, R. Kobayashi, K. Otomo, K. Yabuuchi, A. Kimura, Microstructure and mechanical properties of HAZ of RPVS clad with duplex stainless steel, Journal of Nuclear Materials 545 (2021) 152756.
6. J. Drouet, L. Dupuy, F. Onimus, F. Mompiou, S. Perusin, A. Ambard, Dislocation dynamics simulations of interactions between gliding dislocations and radiation induced prismatic loops in zirconium, Journal of Nuclear Materials 449 (2014) 252 – 262.
7. A. Arsenlis, M. Rhee, G. Hommes, R. Cook, J. Marian, A dislocation dynamics study of the transition from homogeneous to heterogeneous deformation in irradiated body-centered cubic iron, Acta Materialia 60 (2012) 3748 – 3757.
8. W.G. Wolfer, T. Okita, D.M. Barnett, Motion and Rotation of Small Glissile Dislocation Loops in Stress Fields, Phys. Rev. Lett. 92 (2004) 085507.
9. B. Bakó, E. Clouet, L.M. Dupuy, M. Blétry, Dislocation dynamics simulations with climb: kinetics of dislocation loop coarsening controlled by bulk diffusion, Philosophical Magazine 91 (2011) 3173 – 3191.
10. M. Topping, T. Ungár, C.P. Race, A. Harte, A. Garner, F. Baxter, S. Dumbill, P. Frankel, M. Preuss, Investigating the thermal stability of irradiation-induced damage in a zirconium alloy with novel in situ techniques, Acta Materialia 145 (2018) 255 – 263.
11. T.D. Swinburne, K. Arakawa, H. Mori, H. Yasuda, M. Isshiki, K. Mimura, M. Uchikoshi, S.L. Dudarev, Fast, vacancy-free climb of prismatic dislocation loops in bcc metals, Sci Rep 6 (2016) 30596.
12. B.V. Cockeram, K.J. Leonard, T.S. Byun, L.L. Snead, J.L. Hollenbeck, The recovery of irradiation damage for Zircaloy-2 and Zircaloy-4 following low dose neutron irradiation at nominally 358°C, Journal of Nuclear Materials 461 (2015) 244 – 264.
13. N. Castin, A. Bakaev, D. Terentyev, M.I. Pascuet, G. Bonny, Understanding why dislocation loops are visible in transmission electron microscopy: The tungsten case, Journal of Nuclear Materials 555 (2021) 153122.
14. F. Kroupa, P.B. Price, "Conservative climb" of a dislocation loop due to its interaction with an edge dislocation, Philosophical Magazine 6 (1961) 243 – 247.
15. J.A. Turnbull, The coalescence of dislocation loops by self climb, Philosophical Magazine 21 (1970) 83 – 94.
16. F. Liu, A.C.F. Cocks, E. Tarleton, A new method to model dislocation self-climb dominated by core diffusion, Journal of the Mechanics and Physics of Solids 135 (2020) 103783.
17. F. Liu, A.C.F. Cocks, E. Tarleton, Dislocation climb driven by lattice diffusion and core diffusion, Journal of the Mechanics and Physics of Solids 176 (2023) 105300.
18. S.L. Dudarev, A.P. Sutton, Elastic interactions between nano-scale defects in irradiated materials, Acta Materialia 125 (2017) 425 – 430.
19. T. Okita, S. Hayakawa, M. Itakura, M. Aichi, S. Fujita, K. Suzuki, Conservative climb motion of a cluster of self-interstitial atoms toward an edge dislocation in BCC-Fe, Acta Materialia 118 (2016) 342 – 349.
20. T. Aliev, M. Kolesnik, Kocks-Mecking-Estrin type model for high-temperature creep of Zircaloy-4, Journal of Nuclear Materials 561 (2022) 153534.
21. V.P. Ramunni, A.M.F. Rivas, Diffusion calculations with two atomic models in h. c. p Zr-Nb diluted alloys, Materials Chemistry and Physics 197 (2017) 163 –180.
22. H. Wen, C.H. Woo, Temperature dependence and anisotropy of self- and mono-vacancy diffusion in α-Zr, Journal of Nuclear Materials 420 (2012) 362 – 369.
23. M.E. Kassner, Chapter 2 — Five-Power-Law Creep, in: M.E. Kassner (Ed.), Fundamentals of Creep in Metals and Alloys (Third Edition), Butterworth-Heinemann, Boston, 2015, pp. 7–102.
24. T.A. Hayes, M.E. Kassner, Creep of zirconium and zirconium alloys, Metall Mater Trans A 37 (2006) 2389 – 2396.